Pathway for Insertion of Amphiphilic Nanoparticles into Defect-Free Lipid Bilayers from Atomistic Molecular Dynamics Simulations[†]

Reid C. Van Lehn and Alfredo Alexander-Katz[*]

Gold nanoparticles (NPs) have been increasingly used in biological applications that involve potential contact with cellular membranes. As a result, it is essential to gain a physical understanding of NP-membrane interactions to guide the design of next-generation bioactive nanoparticles. In previous work, we showed that charged, amphiphilic NPs can fuse with lipid bilayers after contact occurs between protruding solvent-exposed lipid tails and the NP monolayer. Fusion was only observed at the high-curvature edges of large bilayer defects, but not in low-curvature regions where protrusions are rarely observed. Here, we use atomistic molecular dynamics simulations to show that the same NPs can also fuse with low-curvature bilayers in the absence of defects if NP-protrusion contact occurs, generalizing the results of our previous work. Insertion occurs without applying biasing forces to the NP, driven by the hydrophobic effect, and involves the transient generation of bilayer curvature. We further find that NPs with long hydrophobic ligands can insert a single ligand into the bilayer core in a manner similar to the binding of peripheral proteins. Such anchoring may precede insertion, revealing potential methods for engineering NP monolayers to enhance NP-bilayer fusion in systems with a low likelihood of lipid tail protrusions. These results reveal new pathways for NP-bilayer fusion and provide fundamental insight into behavior at the nano-bio interface.

1 Introduction

Gold nanoparticles (NPs) with core diameters smaller than 10 nanometers are regarded as potentially powerful tools for biomedical applications including targeted drug delivery, bioimaging, and biosensing because their properties and interactions with the biological milieu can be tuned by engineering the composition of a protecting surface monolayer[1–3]. Notably, there is strong interest in developing novel NPs that favorably interact with cellular membranes in order to achieve the intracellular delivery of cargo without toxic side effects. As a result, several experimental[1] and simulation[4] studies have explored this nano-bio interface to identify how NP surface properties influence cellular uptake. For example, recent work has studied the effect of NP properties on endocytosis[5,6], membrane disruption[7,8], and direct bilayer penetration by hydrophobic NPs[9]. NPs with amphiphilic surface properties have garnered particular notice due to their similarity to lipids. Lipids are biological amphiphilies that form the major structural component of the cell membrane and limit the passive diffusion of charged groups through the bilayer. Despite the barrier properties of the membrane, amphiphilic membrane proteins are able to stably integrate within bilayers by preferentially exposing uncharged, hydrophobic side chains to the bilayer core and exposing charged side groups to surrounding solvent[10]. The physicochemical similarity between amphiphilic NPs, amphiphilic bilayer, and amphiphilic transmembrane proteins thus suggests that such stable membrane integration may also be possible for synthetic NPs.

In recent work, we combined multiple simulation and experimental methodologies to demonstrate that charged, amphiphilic, ligand-coated gold NPs can spontaneously insert into and fuse with lipid bilayers[11–15]. Using an implicit bilayer, implicit solvent simulation method, we calculated the free energy change for incorporating an amphiphilic NP into the membrane as a function of the NP size and monolayer composition[11,13,14]. The free energy change for such NP-bilayer fusion was found to be favorable if the NP core diameter was below a monolayer-dependent size threshold, a result confirmed with experiments using model lipid membranes[11,12]. Moreover, the same size thresholds correlated with NP uptake in cells, even at low temperatures where endocytosis is inhibited, indicating that fusion is a precursor to cell internalization[11]. After fusion, the NPs exhibited a configuration resembling transmembrane protein facilitated by the fluctuations of charged end groups to the aqueous interface.

We further used atomistic molecular dynamics simulations to identify a possible kinetic pathway for such fusion mediated by interactions between the same NPs and the edges of large bilayer defects[15]. Using a lipid "ribbon" containing two high-

curvature edges and two planar faces, the simulations found that NPs were able to rapidly ($<$ 100 ns) insert into the bilayer through the ribbon edges without the aid of any biasing force [15]. No insertion was observed through the planar bilayer face over a much longer timescale (500 ns). Experiments on supported lipid bilayers confirmed that NPs could spontaneously insert at the edges of large bilayer defects but not in perfectly planar bilayers, agreeing with the unbiased simulation results [15]. The simulations showed that insertion occurred after contact between hydrophobic ligand backbones in the NP monolayer and a hydrophobic lipid tail that had stochastically protruded into solvent at the ribbon edge [15]. NP-protrusion contact was found to be a high energy transition state due to the unfavorable solvation of the hydrophobic lipid tail that could be relaxed by sequestering the tail within the NP monolayer, triggering insertion. The free volume accessible to lipid tails in regions of high curvature allowed protrusions to appear within simulation timescales at the ribbon edge, but not the planar face of the ribbon, explaining the simulation observations.

While the previous atomistic simulations did not show unbiased NP-bilayer insertion in the absence of defects, previous experiments have established that NPs are capable of fusing with vesicles [11] which in principle should exhibit more tail protrusions than planar supported lipid bilayers due to the curvature and fluctuations of the unconstrained bilayer surface [17]. Moreover, NP-vesicle fusion was observed experimentally without allowing the passage of membrane-impermeable dyes, implying that large defects are not necessary for NP insertion [11]. Based on these prior findings, we hypothesize that contact with lipid tail protrusions can also lead to the fusion of NPs with defect-free bilayers.

In this work, we use a novel atomistic molecular dynamics workflow to determine if NP-protrusion contact is sufficient to trigger insertion in low-curvature lipid bilayers. We first introduce lipid tail protrusions into the planar face of a lipid ribbon in order to obtain system configurations with NP-protrusion contact. Many unbiased, short simulations are then launched from this putative transition state to determine if NP-bilayer fusion is possible without contact with bilayer defect edges. We find that a NP can spontaneously insert into the bilayer without applying biasing forces to the NP directly, confirming a thermodynamic driving force for insertion related to the reduction of the hydrophobic surface area to water [11,13]. The pathway for insertion involves initial mixing of hydrophobic lipid tails and hydrophobic ligands to form a stalk-like intermediate that resembles the onset of vesicle-vesicle fusion [18], followed by the generation of transient bilayer curvature that decays as hydrophobic ligands extend into the bilayer. By comparing two NP compositions, we also identify an alternative "anchoring" behavior in which a single hydrophobic ligand intercalates within the bilayer core before insertion oc-

curs after a protrusion spontaneously appears. This pathway is similar to the initial binding of peripheral proteins and suggests opportunities to engineer ligands that encourage bilayer fusion. These results provide significant physical insight into the kinetic pathway for NP-bilayer fusion and generalizes the previous findings of protrusion-mediated insertion at defect edges to low-curvature, defect-free bilayers [15]. As amphiphilic NPs are already being tested for potential biomedical applications [19,20], we expect that our findings will be critical for optimizing NPs to exploit the membrane fusion pathway.

2 Methods

2.1 System description and preparation

To determine if contact with lipid tail protrusions is sufficient to drive NP insertion, we used atomistic molecular dynamics simulations to model the interactions between a NP and the planar face of a dioleoylphosphatidylcholine (DOPC) lipid "ribbon" containing tail protrusions. Each NP had a gold core with diameters of 2.0 nm and was protected by a mixed-ligand monolayer with a composition of either MUS:OT or MUS:HDT ligands in a 1:1 ratio. MUS (mercaptoundecane sulfonate) has an 11-carbon alkyl backbone and is end-functionalized with an anionic sulfonate group which was assigned a net -1 charge. OT (octanethiol) and HDT (heptadecanethiol) are both purely hydrophobic with 8 and 17-carbon backbones respectively. The combination of the charged, hydrophilic MUS end groups and hydrophobic alkane backbones yields amphiphilic surface properties. Chemical structures of all three ligand species and the DOPC lipid are shown in Fig. 1a. The NP core was approximated as uniformly spherical and the monolayer was grafted at a density of 4.62 ligands/nm^2 for a total of 58 ligands, consistent with values in the literature [21]. Each NP was equilibrated for 100 ns at 310 K and 1 bar in a 150 mM NaCl salt solution to represent typical biological conditions. The temperature was maintained using a velocity-rescale thermostat with a time constant of 0.1 ps. The pressure was controlled using an isotropic Parrinello-Rahman barostat with a time constant of 2.0 ps and an isothermal compressibility of 4.5 $\times 10^{-5}$ bar^{-1}. Additional details on the NP parameterization are included in the ESI†.

A lipid ribbon is a bilayer that is fully periodic along one simulation vector but has two edges separated by solvent as shown in Fig. 1b. This morphology was chosen based on preliminary results (see Fig. S1†) in order to create free boundaries that allow the two bilayer leaflets to asymmetrically expand and bend. The generation of such membrane curvature is inhibited in conventional box-spanning bilayers with periodic boundary conditions [22] but would be possible in experimental lipid systems [23]. Similar structures with free boundaries, such as bilayer patches, have also been used frequently to model
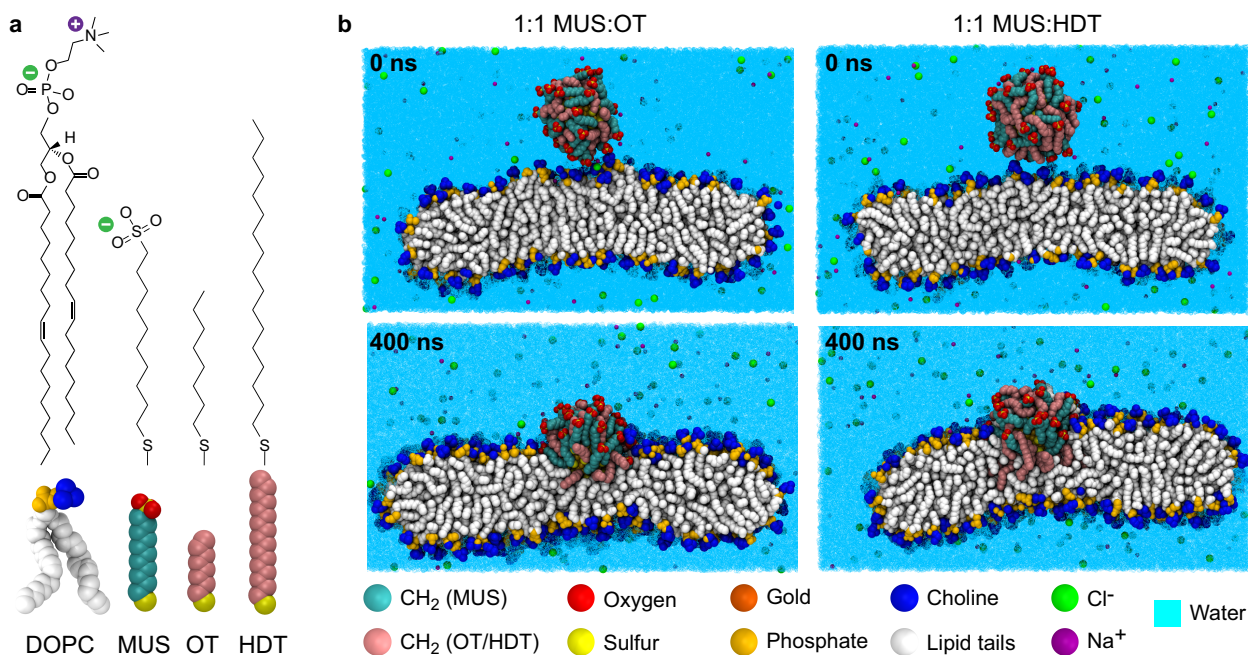
Fig. 1 Summary of simulation components. **a** Chemical structures and simulation representations of DOPC lipid and three monolayer ligands. **b** Snapshots of both 1:1 MUS:OT (left) and 1:1 MUS:HDT (right) NPs in their initial configurations above the lipid ribbon and after 400 ns of simulation following insertion (see text). Atoms are colored according to the legend below. Water and ions are not shown in the remainder of the simulation images for visual clarity. All snapshots were generated with Visual Molecular Dynamics [16].

curvature induced by membrane proteins [22,24–28] and a recent study of NP-bilayer interactions has pointed to the geometric constraints imposed by fully-periodic bilayers [8]. While the effect of free boundaries could be achieved by simulating a much larger bilayer [29], such an approach would be too computationally demanding for the atomistic resolution employed here. Moreover, previous studies have shown that the middle, planar portion of the ribbon has identical structural properties to conventional box-spanning bilayers [30]. Positioning NPs above the middle of a lipid ribbon thus mimics the approach of NPs to a large defect-free bilayer or vesicle system that is able to bend and expand. We emphasize that the ribbon construction is used only to overcome computational limitations and is not meant to represent a bilayer with large defects as the ribbon edges play no role in the observed NP-bilayer interactions, unlike in previous work [15]. Additional discussion on the need for free boundaries to properly model NP-bilayer insertion is included in the ESI and Fig. S1†.

The ribbon was assembled by duplicating a previously-equilibrated 200 lipid bilayer along the x-axis of the simulation box and adding water to increase the x box vector by an additional 10 nm [15,30]. The 400 lipid bilayer was then equilibrated for 100 ns at 310 K and 1 bar pressure in a 150 mM NaCl salt solution. The temperature was controlled using a velocity-rescale thermostat with a time constant of 0.1 ps. The

pressure was maintained with an anisotropic Berendsen barostat with a time constant of 5.0 ps and an isothermal compressibility of 4.5×10^{-5} bar^{-1}. The bilayer was aligned such that the free boundaries were parallel to the y-axis; accordingly, the box dimension was also fixed in the y-dimension to maintain the ribbon structure while the x- and z-dimensions could be resized under the action of the barostat. To minimize the exposure of the hydrophobic lipid tails to water, lipid head groups migrated to form high-curvature edges at the solvent-exposed ribbon sides during equilibration. An equilibrated NP and its counterions were then inserted into the simulation box and excess water was removed from the system to improve the efficiency of calculations, leaving a total simulation box size of 21.26 nm by 8.20 nm by 12.47 nm. These dimensions were sufficient to have at least 2.0 nm of separation between the NP and the periodic image of the ribbon along the z-axis and at least 3.5 nm between the edges of the ribbons across the periodic box, both values larger than the force field cutoffs. The final system contained 400 lipids, 47,974 water molecules, 167 Na$^+$ ions, and 138 Cl$^-$ ions. A brief 5 ns equilibration was performed after the introduction of the NP. Fig. 1b shows snapshots of both the 1:1 MUS:OT and 1:1 MUS:HDT systems following the excess water removal and equilibration, then again after 400 ns of additional simulation (as detailed in the Results section below).

The GROMOS 54a7 united atom force field was used to model the lipids, ions, and NPs in conjunction with the SPC water model following previous work [15,31–34]. Electrostatic interactions were calculated using the smooth particle-mesh Ewald (PME) method with fourth order interpolation and a 0.12 nm grid size. The neighbor list cutoff, short-range electrostatic cutoff, and Lennard-Jones cutoff were all set to 1.0 nm to match recent parameters recommended for using PME with the GROMOS 54a7 force field [35]. The simulation timestep was set to 2 fs and molecular dynamics was performed using a leap-frog integrator. Bonds were constrained using the LINCS algorithm [36]. All simulations were performed using Gromacs v4.6.3 [37].
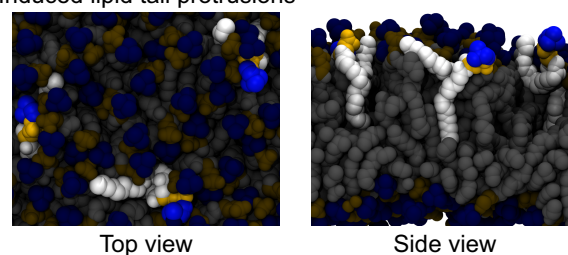
2.2 Workflow for inducing NP-protrusion contact

The goal of this work is to determine if a NP can insert into a low-curvature, defect-free lipid bilayer after contacting lipid tail protrusions [15]. However, tail protrusions are thermodynamically unfavorable (see Results below) and as a result are rarely observed in planar bilayers, possibly explaining why NP insertion was observed in long timescale experiments but not in previous unbiased simulations [11,15]. We thus developed a novel workflow to achieve NP-protrusion contact with a particular emphasis on minimizing the amount of bias to the system. Notably, our workflow does not require the application of any biasing forces other than the use of an umbrella potential to generate the initial protrusions, and in particular does not involving applying forces to the NP itself.

First, three protrusions were introduced in the ribbon by applying an umbrella potential to pull lipid atoms along the bilayer normal to a distance of 0.3 nm beyond the plane formed by the phosphorus atoms in the upper monolayer (additional details are included in the Supplementary Material†). The potential was applied only to the last atom in the *sn*-1 tail of each lipid in order to induce a protrusion in a "splay" configuration similar to what has been previously implicated in driving vesicle fusion [38–40] or NP insertion at ribbon edges [15]. We chose to force three protrusions in order to increase the likelihood of contact with the NP during the "searching" simulations described below. The chosen lipids were positioned in the middle region of ribbon, where the structural properties match conventional box-spanning bilayers [30], and were spatially separated in the top monolayer to prevent interactions between protrusions. Fig. 2 shows snapshots of the three protruding lipid tails from the top and side. The NP was then allowed to move freely for 40 ns with the biasing potential maintained to prevent protrusions from relaxing. Electrostatic interactions between the charged MUS end groups and the zwitterionic lipid tails attracted the NP to the bilayer surface such that it was not necessary to apply additional forces to the NP to maintain close surface association. During these "search-

ing" trajectories, the number of hydrophobic contacts, H_C, between the bilayer and the NP monolayer was monitored. H_C was defined as the total number of hydrophobic lipid tail atoms within 0.5 nm of any hydrophobic atom in the NP monolayer, a distance approximately equal to the diameter of an aliphatic group in the united atom model plus the diameter of a water molecule. Six searching simulations were run for each of the two NP compositions.

a Induced lipid tail protrusions

Top view   Side view

b NP introduced in vicinity of protrusions

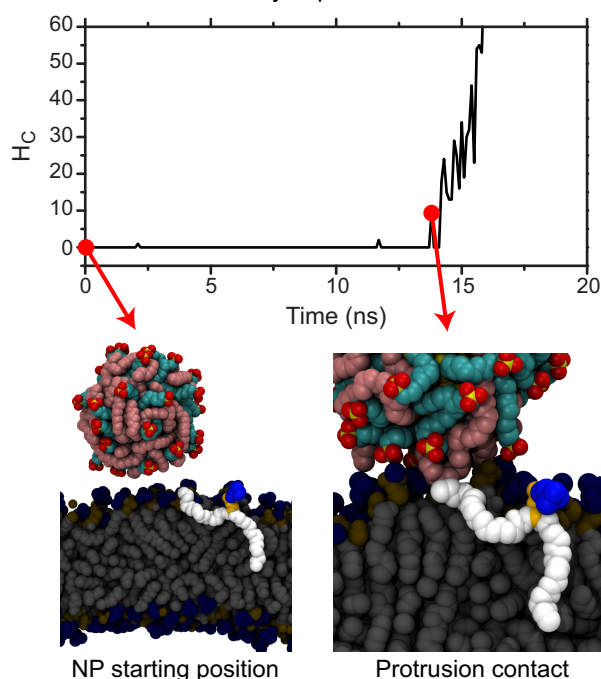NP starting position   Protrusion contact

Fig. 2 Workflow for inducing NP-protrusion contact. Snapshots are shown for a 1:1 MUS:HDT NP. **a** Three protrusions (highlighted) were pulled to a distance of 0.3 nm above the plane of phosphorus atoms by applying an umbrella potential. Snapshots illustrate their in-plane separation and the extent of pulling. Some lipids are removed to aid in visualizing the protruding tails. **b** Searching simulations were launched from a NP positioned above the middle, planar region of the ribbon and were monitored for NP-protrusion contact by measuring H_C as a function of time. The configuration corresponding to initial NP-protrusion contact (red dot and arrow) was extracted as a starting point for probing simulations.

Fig. 2b shows the time evolution of H_C during an example searching simulation. H_C stays near zero as the NP traverses the bilayer surface until rapidly increasing when the NP eventually encounters a protrusion. From these simulations, four configurations corresponding to initial NP-protrusion contact with varying values of H_C were extracted for each NP composition. The circled value and accompanying snapshot illustrate an example extracted configuration with NP-protrusion contact. Notably, all searching simulations that led to NP-protrusion contact eventually ended with the NP fusing with the bilayer (as shown by the large increase in H_C in Fig. 2), indicating that if a protrusion is continuously forced NP insertion occurs readily. Fig. S2†shows snapshots of all configurations extracted for both NP types.

Next, 20 short, unbiased "probing" trajectories were launched from each of the configurations extracted from the searching simulations for a total of 80 trajectories per NP composition. Prior to each probing trajectory, the velocities of all atoms were randomized from a Maxwell-Boltzmann distribution at 310 K. The simulations were then run without constraints to observe unbiased NP/lipid dynamics. After 5 ns, each probing trajectory was classified into one of four categories as described below in the Results. Three probing simulations for each NP composition were extended to 400 ns to study longer timescale insertion behavior. Finally, one trajectory for each NP composition was run for 400 ns with the NP introduced above a ribbon without any induced protrusions as a control. All simulations - searching, probing, and extended - used the same simulation parameters as the equilibration of the bilayer ribbon.

3 Results and Discussion

3.1 NPs observed to insert into bilayer in large number of probing simulations

The short, 5 ns probing simulations were sorted into four different outcomes based on the number of NP-bilayer hydrophobic contacts, H_C, and visual inspection. If H_C dropped to zero, the NP was classified as "in solution" due to the relaxation of the protrusion without continue NP contact. If $H_C > 100$, the NP was classified as "inserted" as the rapid rise in H_C indicated the onset of NP-bilayer fusion. For $0 < H_C < 100$, two possibilities were found. First, the NP could be "anchored", in which case the protrusion relaxed back into the bilayer but a hydrophobic ligand from the NP inserted within the hydrophobic core. This behavior was only identified for the MUS:HDT NPs. Second, the NP could be "uncommitted", in which case the protrusion did not relax within 5 ns and remained in contact with the NP but without triggering the large increase in H_C associated with insertion. All initially uncommitted trajectories were extended an additional 5 ns to see if the protrusion
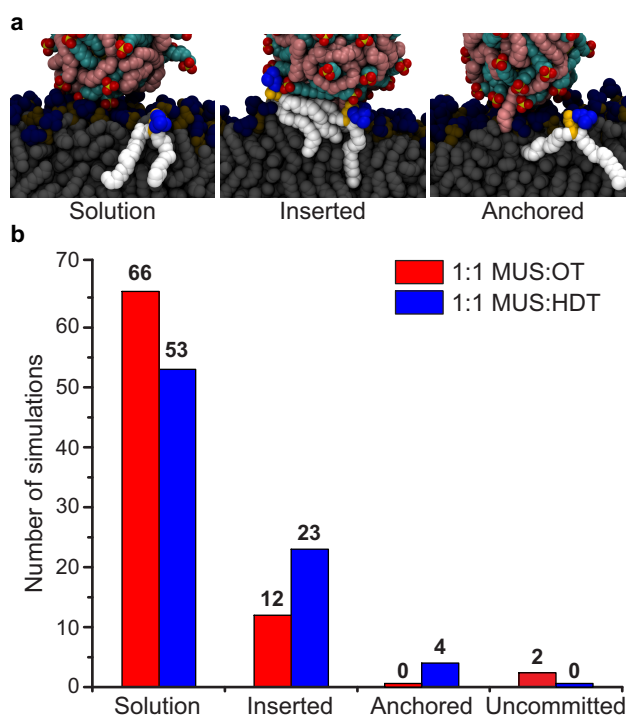

Fig. 3 Summary of 5 ns unbiased probing simulations. **a** Snapshots of three possible outcomes of probing simulations. The original protruding lipid is highlighted in each image. For the "inserted" state, all lipids in hydrophobic contact with the NP are highlighted. **b** Number of observations of each outcome for both NP types from 80 total probing simulations per particle, 20 for each of the starting configurations in Fig. S2†.

relaxed or insertion occurred, and if not were then classified as uncommitted. Snapshots of the solution, inserted, and anchored outcomes are shown in Fig. 3a.

Fig. 3b compares the relative frequency of the four possible probing simulation outcomes from the 80 total probing simulations launched for each NP composition. A large number of simulations - 12 for MUS:OT, 23 for MUS:HDT - began to insert into the bilayer within the 5 ns interval. These results definitively confirm that contact with a single protruding lipid tail is sufficient to drive the insertion of an amphiphilic NP into a lipid bilayer, generalizing previous findings of protrusion contact driving NP insertion through high-curvature defect edges [15]. Moreover, these observations of insertion without the application of biasing forces to the NP indicate that NP-bilayer fusion is thermodynamically favorable once the barrier to initial protrusion contact is overcome; we also never observe a decrease in H_C for NPs that begin to insert. However, the majority of the simulations ended with the relaxation of the protrusion without the NP inserting or anchoring, indicating that even after NP-protrusion contact insertion

is still uncommon. The MUS:HDT NPs inserted with more frequency than MUS:OT NPs despite similar values of H_C for the extracted configurations shown in Fig. S2†. The larger number of fusion events may reflect a stronger hydrophobic driving force due to the longer hydrophobic ligands. Finally, a small number of simulations ended with an anchored ligand, although this only occurred for the MUS:HDT NPs.

The onset of insertion was characterized by the mixing of hydrophobic lipid tails and monolayer ligands at the NP-bilayer interface. Fig. 4 shows the increase in H_C along with representative snapshots during a 5 ns probing simulation that ended in insertion. In each snapshot, all lipids and ligands that have at least one atom in hydrophobic contact are highlighted. The snapshots show that this lipid/ligand mixing occurred as: (1) the protruding lipid tail extended farther out of the bilayer and into the NP monolayer, (2) monolayer ligands deformed to maximize contact with the protrusion, and (3) additional lipids and ligands added to the growing site of lipid/ligand mixing. Similar observations were made in multiple other simulations of both MUS:OT and MUS:HDT NPs (see Fig. S3 for an example of MUS:HDT insertion†). The protrusion relaxed before this collective lipid/ligand rearrangement could occur in probing simulations that ended without insertion. The fusion pathway qualitatively mimics the increase in hydrophobic contact associated with stalk formation during vesicle-vesicle fusion when lipids from apposed monolayers mix in the intervening solvent region[18,39,40]. Here, hydrophobic ligands act like lipid tails in contributing to the nascent stalk. Similarly, protrusion contact is also associated with the pre-stalk transition in vesicle fusion[38–41].

3.2 NP insertion generates bilayer curvature, decreases solvent-accessible surface area

From the set of probing simulations that ended in insertion, three trajectories were continued for 400 ns for each NP composition to observe further insertion dynamics. Fig. 5 shows the hydrophobic solvent-accessible surface area (SASA) of the NP as a function of time for the first 150 ns of two trajectories for each NP composition. The SASA has previously been shown to scale approximately linearly with the free energy penalty for exposing hydrophobic material to water[42]. Starting from the time of first NP-protrusion contact, the SASA monotonically decreased for both NP types before beginning to plateau after 150 ns. For comparison, the dashed horizontal lines indicate the average values of the SASA for the NPs over the last 100 ns of the 400 ns trajectories. The decrease in the SASA confirms the strong hydrophobic driving force for insertion, agreeing with previous work[11,13,15], with a greater decrease exhibited by the MUS:HDT NPs. In contrast, control simulations with NPs placed above bilayers without induced protrusions did not demonstrate NP-bilayer fusion within 400
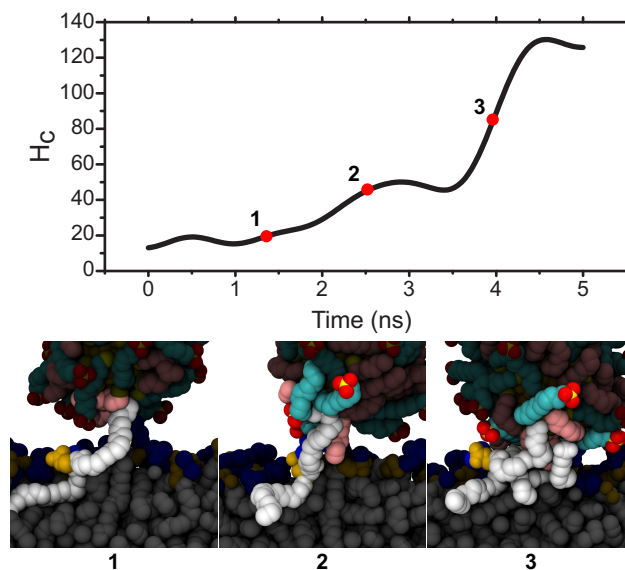

Fig. 4 Features of first 5 ns of insertion following protrusion contact. The number of hydrophobic contacts between the NP and bilayer, H_C, is shown along with representative snapshots. The plot is smoothed with a fast Fourier transformation filter to remove components with frequencies above a 0.0125 ns^{-1} cutoff. Lipids and ligands in hydrophobic contact are highlighted in each image.

ns in the absence of initial NP-protrusion contact (Fig. S4†).

Fig. 5 shows representative snapshots of the MUS:OT NP from trajectory 1 with similar snapshots of a MUS:HDT NP presented in Fig. S3†. At 5 ns, corresponding to the final time in Fig. 4, the NP still had minimal hydrophobic contact with lipid tails reflected in the small decrease in the SASA. By 25 ns, the NP began to insert into the top monolayer of the bilayer, inducing significant curvature (see also zoomed-out images in Fig. S3†). This behavior is consistent with studies of bilayer bending induced by peripheral proteins that shallowly insert into the membrane and preferentially expand only the top bilayer leaflet[43]. The formation of such curvature may contribute to why insertion was not observed experimentally in planar supported bilayers in previous work[15], as the close proximity of the substrate likely inhibits such bending[44]. The NP core continuously moved toward the bilayer midplane as the SASA decreased (see Fig. S5†), leading to a relaxation of generated curvature by 150 ns as the NP core inserted more deeply into the bilayer. This behavior is again consistent with previous findings that showed that curvature is maximized when a protein is inserted near the bilayer head groups and decreases as the protein moves closer to the bilayer midplane[43]. The curvature fully relaxed by 400 ns (see Fig. 1). Additional plots of the SASA and distance of the NP from the bilayer center for the full 400 ns are shown in Fig. S5†.

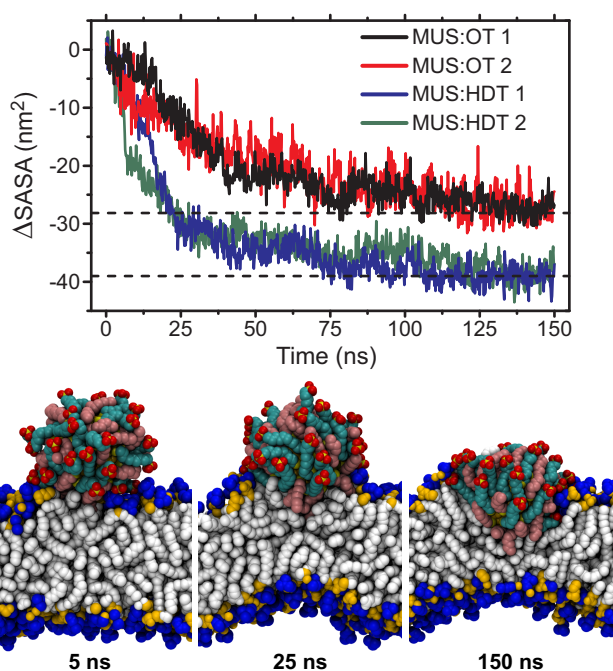During insertion, the hydrophobic OT/HDT ligands ex-

Fig. 5 Insertion pathway for both NP compositions. The change in the SASA for the first 150 ns after NP-protrusion contact is plotted for MUS:OT and MUS:HDT insertion trajectories. The dashed horizontal lines indicate the average value of the SASA between 300-400 ns for each NP composition. Snapshots from the MUS:OT 1 trajectory (black line) are shown. Snapshots from MUS:HDT 1 are shown in Fig. S3†.

tended into the bilayer core. In contrast, the MUS ligands deformed toward the nearest aqueous interface to maintain the solvation of the charged end groups. This behavior, referred to as "snorkeling" when observed in protein side chains[45], is critical for NP insertion by allowing the amphiphilic NPs to effectively rearrange their surface properties to avoid the exposure of charge to the low dielectric constant bilayer core[11,13,15,46]. The snorkeling of the MUS ligands depends on their flexibility, a key feature of the alkanethiol ligands that can be captured using the atomistic resolution used here. In contrast, other simulation models of NP-bilayer interactions which neglect this accurate treatment of ligand fluctuations or ligand charges have observed direct charged ligand-lipid core contact, a high energy, unstable state that was not observed in these simulations[47–50]. We thus emphasize that the atomistic modeling methodology used in this work is necessary to accurately resolve details of NP-bilayer fusion, and particularly the ligand fluctuations that facilitate stable insertion. Charged end groups also never crossed the bilayer, leading to significant strain on the MUS ligands grafted to positions farthest from the aqueous interface. The sequence of snapshots thus illustrates that insertion occurred irreversibly after protrusion con-

tact, generated transient bilayer curvature, and ended with the NP partially embedded within the bilayer but with all charged end groups still snorkeled toward one side of the bilayer.

3.3 Alternative fusion pathway involves initial ligand anchoring

In a small number of probing simulations, we also identified a separate pathway characterized by a single hydrophobic ligand inserting into the bilayer without full NP fusion occurring, effectively "anchoring" the NP to the bilayer. Anchoring was only observed for four of the MUS:HDT NP simulations (Fig. 3). One MUS:HDT anchored trajectory was continued for 400 ns. Fig. 6 shows the change in the SASA with accompanying snapshots for the first 100 ns of the anchored trajectory, labeled as MUS:HDT 3, and compared to an insertion trajectory from Fig. 5. The major difference between the two behaviors is a plateau region in which the SASA for the anchored simulation remained nearly constant until beginning to decrease after approximately 15 ns. The snapshots illustrate the role of the long hydrophobic HDT ligands in facilitating this secondary pathway. The snapshot at 5 ns shows a single ligand extending through the head group region of the bilayer and intercalating within the lipid tail region. Anchoring allowed the NP to remain in close contact with the membrane surface until a spontaneous lipid protrusion occurred at 11 ns. The protruding tail aligned with the inserted ligand and made contact with the monolayer, initiating the slow decrease of the SASA. The snapshot at 20 ns shows the addition of a second hydrophobic ligand to the nascent stalk and the continued deformation of lipid tails analogous to the findings in Fig. 4. The SASA decreased significantly once these additional molecules came into contact until eventually plateauing in a conformation effectively identical to the end point of the non-anchored trajectory in Fig. 5 and Fig. S3†. The anchored insertion pathway thus utilized a distinct starting state but still proceeded after the appearance of a lipid tail protrusion and ended in a similar final configuration.

3.4 Protrusions occur spontaneously near anchored NPs

The spontaneous appearance of a protrusion 11 ns after ligand anchoring is surprising given the small frequency with which such protrusions are observed. To confirm that tail protrusions are rare events that should be expected infrequently, we computed the potential of mean force (PMF) for inducing a protrusion. The PMF measures the free energy change associated with the formation of a protrusion and was calculated from umbrella sampling simulations using the weighted-histogram analysis method[51]. Full details on the calculation of the PMF are in the Supplementary Material†.

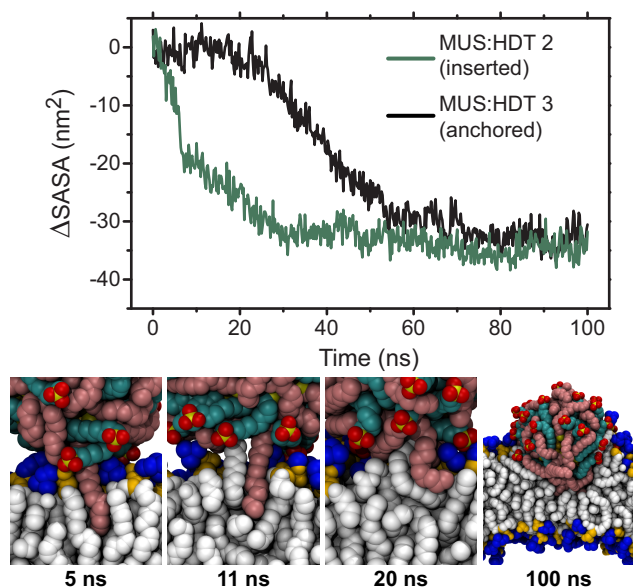Fig. 7 shows the PMF in units of kT for pulling a lipid

Fig. 6 NP insertion following ligand anchoring. The change in SASA is shown for the first 100 ns of an trajectory initiated from an anchored configuration (MUS:HDT 3) and compared to a trajectory from Fig. 5 (MUS:HDT 2). Snapshots from the MUS:HDT 3 trajectory are shown.

tail into solvent as a function of the distance of the pulled tail atom from the bilayer center of mass. For comparison, the electron densities of the hydrophobic lipid tails, charged phosphate head groups, and water are also plotted as a function of the same distance. The dashed vertical line indicates the distance to which protrusions were pulled during the searching simulations (0.3 nm beyond the phosphate group peak). From the PMF, the free energy cost for inducing protrusions to this distance is approximately 10.5 kT. This barrier is comparable to other related membrane processes that occur over experimental timescales. For example, the cost for water crossing a membrane has been estimated as 7.8 - 11.7 kT (at 310 K) depending on the lipid species[52], lipid flip-flop has a barrier of approximately 31.2 to 37 kT[53], and cholesterol flip-flop has a barrier of approximately 7.0 to 16.0 kT[54]. Compared to these processes, it is apparent that the cost for observing a protrusion is sufficiently low that they would be expected to appear in an experimental system in the absence of additional constraints (e.g. the presence of a supporting substrate), but should only be rarely observed in simulations, agreeing with the infrequent increases in H_C found in the control simulations (Fig. S5†). The observation of a spontaneous splay-like protrusion in just 11 ns near the anchored ligand thus suggests that the ligand's presence affects protrusion likelihood.

Comparing the PMF with the electron density plots shows that the main origin of the free energy barrier is contact with an

increasing amount of water as the hydrophobic tail approaches the lipid-solvent interface. This finding is apparent from two regimes of behavior of the PMF - first, the PMF increases approximately linearly in a region dominated by lipid tail density until the slope of the PMF increases coincident with a decrease in tail density and increase in water density. The simulation snapshots in Fig. 7 further emphasize this behavior by showing configurations corresponding to the points labeled on the PMF plot. In each snapshot the pulled lipid is shown with the restrained atom in red, other lipid head groups darkened, other lipid tails omitted for visual clarity, and water as a cyan background. The first snapshot shows the lipid near its equilibrium position. The second image shows that the slope of the PMF increases as the pulled tail approaches the head group region. In snapshot 3a, the pulled bead is in contact with solvent leading to the large increase in free energy. From these observations, we propose that lipid protrusions may spontaneously occur over relatively short timescales near anchored NPs due to a reduction in water exposure. Snapshot 3b is a different angle of the 11 ns snapshot in Fig. 6 with non-anchored ligands removed. This image shows that the protruding lipid extends toward the NP while maintaining contact with the inserted ligand, consistent with a lower solvation penalty. While there would still be a barrier associated with the protruding approaching the interface (i.e. snapshot 2), the lower cost for a protrusion near an anchor explains the observation of a spontaneous protrusion. The red dashed line illustrates the proposed PMF in the presence of the anchor - the hydrophobic contact reduces the barrier, allowing a protrusion to occur on a faster timescale than expected in a pure bilayer.

3.5 Anchoring pathway suggests opportunities for optimized ligand design

The trajectory in Fig. 6 is a single example of an anchored NP that eventually inserted after the spontaneous protrusion of a nearby lipid tail, but in principle the timescale for such a protrusion occurring could be longer than the typical time that the ligand stays within the bilayer. Furthermore, the probing simulations only ended in anchoring behavior for MUS:HDT NPs, not MUS:OT NPs, indicating that longer hydrophobic ligands may be necessary for this behavior (c.f. Fig. 3). To test whether anchoring can persist long enough for protrusions to occur, an umbrella potential was used to pull a single hydrophobic ligand into the bilayer for both MUS:OT and MUS:HDT NPs. Unbiased simulations were then continued from these configurations and H_C was monitored to determine the time until H_C decreased to 0, marking the withdrawal of the inserted ligand and detachment of the NP. 20 of these simulations were launched for the MUS:HDT NP and 10 were launched for the MUS:OT NP. Separately, a set of simulations was run with MUS:HDT NPs where the anchored ligand was
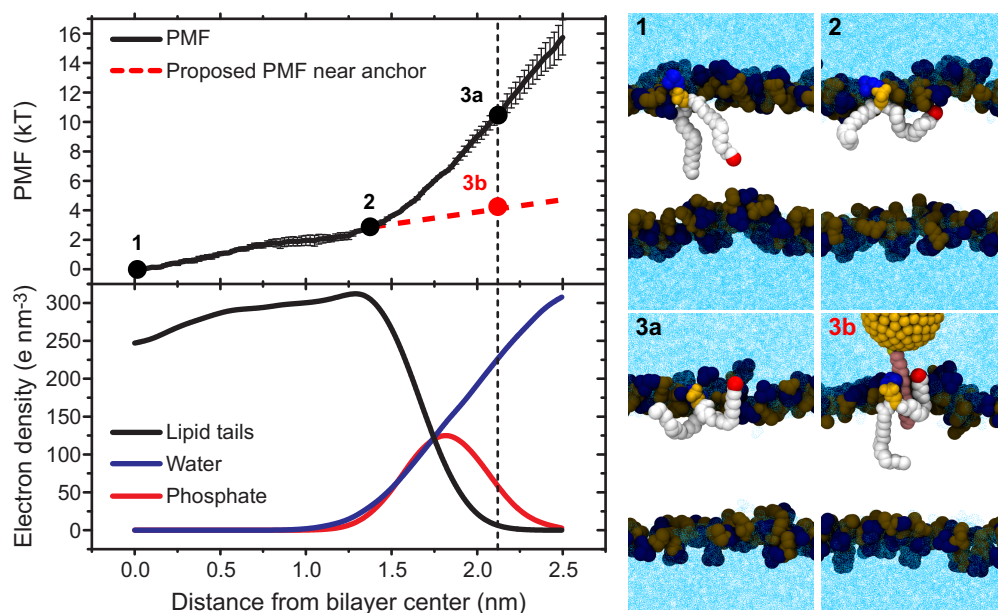
Fig. 7 Potential of mean force for a lipid protrusion from umbrella sampling simulations. The PMF is expressed in *kT* as a function of the distance of the pulled lipid bead from the bilayer center of mass along the z-axis. The electron densities of lipid tails, water, and phosphate are shown projected onto the same axis. The dashed vertical line shows the distance to which lipid tails were pulled to encourage NP contact (see Fig. 2). Representative snapshots of system configurations are labeled and shown with the pulled lipid colored in red and other tails removed for clarity. The dashed red line indicates the proposed PMF for a protrusion in the vicinity of an anchored hydrophobic ligand (snapshot 3b).

retained in the bilayer with an umbrella potential and H_C was monitored to determine the time necessary for a protrusion to occur. Full details of these methods and representative snapshots are shown in the Supplementary Material and Fig. S6†.

Fig. 8 summarizes the behavior of the different anchoring simulations. Fig. 8a shows the number of hydrophobic contacts between the NP and bilayer as a function of time for three representative trajectories - one MUS:OT trajectory with no bias, one MUS:HDT trajectory with no bias, and one MUS:HDT trajectory with the anchoring bias maintained. The two unbiased trajectories both have H_C drop to 0, indicating that the NP detached as labeled in the figure. The unbiased MUS:HDT ligand detached several nanoseconds after the MUS:OT ligand. The biased MUS:HDT trajectory shows a large increase in H_C after approximately 8 ns corresponding to a spontaneous lipid protrusion similar to what was observed in Fig. 6. Fig. 8b summarizes the detachment/protrusion times for all simulations as a histogram showing the fraction of simulations in which the NP detached or a protrusion occurred within the specified time range. The results show that all MUS:OT NPs detached in under 10 ns while a significant fraction of MUS:HDT NPs stayed anchored well in excess of 20 ns. For the simulations with enforced ligand insertion, protrusions occurred in under 50 ns for 70% of the simulations, overlapping with the duration of anchoring for the MUS:HDT

NPs. Surprisingly, none of the unbiased simulations ended with spontaneous insertion; however, given the relatively long timescale until protrusions appear this likely just confirms that even with initial anchoring insertion is still an unlikely process.

These results demonstrate that MUS:HDT NPs, and not MUS:OT NPs, can successfully anchor to bilayers for a sufficiently long time that protrusions may spontaneously occur to trigger further insertion. While using the current workflow we only identify anchoring after induced protrusion contact, the control simulations indicate the potential for successful anchoring in longer simulation runs (Fig. S4†). NP-bilayer fusion thus is more probable when NP monolayers include long hydrophobic ligands capable of inserting and enabling the second insertion pathway, providing a means to overcome the kinetic barrier to insertion associated with NP-protrusion contact. Moreover, there are significant similarities between NP anchoring and the binding of amphipathic membrane-bound peripheral proteins. Like the anchored NPs, certain peripheral proteins stably attach to the bilayer by inserting single hydrophobic amino acid residues into the hydrophobic core and particularly into packing defects, or voids, that may arise due to bilayer curvature or certain lipid compositions[55–57]. This analogous binding behavior opens up the possibility of engineering NPs with long hydrophobic ligands to target bi-
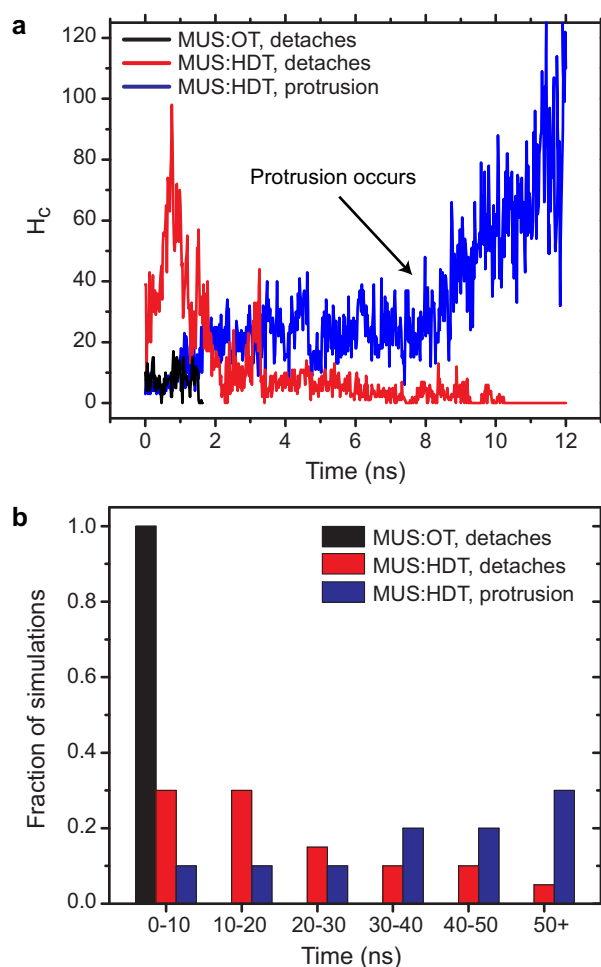
Fig. 8 Timescales for anchor detachment vs. protrusion appearance. **a** Representative trajectories showing H_C during the detachment of a MUS:OT and MUS:HDT NP and the appearance of a protrusion near a MUS:HDT anchored NP. **b** Histogram showing fraction of simulations with detachment/protrusion times within the range specified.

layers with high densities of these hydrophobic defects, such as mixed membranes[58], highly curved liposomes or vesicles[55,58], or bilayers containing negative curvature lipids[59,60]. Future work will exploit this finding to optimize ligand design for enhanced anchoring and bilayer fusion in order to minimize the dependence on the stochastic appearance of protruding lipid tails.

4 Conclusions

Using atomistic molecular dynamics simulations, our results confirm that amphiphilic NPs can insert into the low-curvature face of a lipid ribbon, representative of insertion into defect-free lipid bilayers, if they first come into contact with solvent-exposed lipid tail protrusions. These findings expand upon our previous study in which NP-protrusion contact was identified as the transition state for the insertion of NPs at the edge of bilayer defects[15]. The identified pathway follows several stages: (1) a NP comes into hydrophobic contact with a stochastic tail protrusion, (2) hydrophobic ligands mix with lipid tails at the NP-bilayer interface, (3) the NP shallowly inserts into a single bilayer leaflet, inducing significant bilayer curvature, and (4) the NP approaches the bilayer midplane and the curvature relaxes. The hydrophobic solvent-exposed surface area of the NP monotonically decreases as ligand backbones are sequestered in the bilayer, confirming a strong driving force due to the hydrophobic effect. The first two stages of this pathway also qualitatively resemble the pre-stalk transition and stalk formation stages of vesicle-vesicle fusion[18,39,40], suggesting that the same considerations that affect vesicle fusion likelihood may influence NP-bilayer fusion as well. We also observe a second anchoring pathway in which the first stage of insertion involves the intercalation of a single hydrophobic ligand in the bilayer core, reminiscent of the binding of peripheral proteins. This finding reveals how ligand design may maximize the likelihood of NP-bilayer fusion in membranes with hydrophobic packing defects. Finally, no significant membrane disruption, such as pore formation, was observed in any simulations, agreeing with observations of non-disruptive fusion in vesicles[11], black lipid membranes[12], and previous cell studies[61]. Recent observations from different groups using a variety of experimental techniques have also demonstrated similar fusion behavior in related NP systems[62–64] implying that this pathway may generalize to a variety of NP compositions.

It is important to note several methodological issues identified in this work that could be important in the study of related NP-bilayer interactions[8,48–50]. Most importantly, it is clear that careful consideration must be given to the choice of reaction coordinate when calculating free energy changes for this insertion process. Our simulations clearly indicate that: (1) there is a barrier that prevents immediate NP-bilayer insertion in unbiased simulations, (2) after NP-protrusion contact, bilayer insertion can proceed irreversibly without further bias, and (3) charged ligand end groups do not translocate across the bilayer, indicating another barrier that must be overcome to reach a fully transmembrane state[11,15,34]. The distance between the NP and bilayer center is not a sufficient reaction coordinate to capture all of these effects; it does not resolve the initial protrusion event or barriers to end group translocation. However, recent studies have shown PMFs that are solely a function of the NP-bilayer distance[48–50], and thus neglect these orthogonal reaction coordinates. For example, the PMFs in the work by Li et al.[48] and Gkeka et al.[49] both decrease monotonically with a decrease in the NP-bilayer dis-

tance without exhibiting any barrier to insertion. The former study required an external force on the NP to achieve insertion, indicating that the orthogonal reaction coordinate and corresponding barrier associated with the appearance of a protrusion was neglected. In contrast to these studies, a very recent paper by Gkeka et al.[50] shows a monotonically increasing PMF as the NP-bilayer distance decreases, suggesting that insertion should never occur. The same study also observed that systems with NPs embedded in the bilayer were stable for microsecond timescales, seemingly contradicting the PMF, and agreeing with our atomistic study of embedded NPs[34]. This discrepancy is due to two reasons: their PMF includes contributions from high-energy states where charged groups were exposed to the bilayer and they did not consider barriers related to the distribution of charged ligands on either side of the bilayer. We thus stress that while the NP-bilayer distance may appear to be a logical reaction coordinate for this insertion process, only considering this distance misses the subtle interplay of lipid and ligand fluctuations discussed in this work. It is also critical to emphasize the need for an accurate representation of ligand flexibility and end group electrostatics. Here we use an atomistic model for the NP ligands and accurate electrostatic interactions that resolve the difference in dielectric constant between the bilayer interior and aqueous solution and corresponding free energy cost for exposing charges to a low dielectric environment. In contrast, studies using the dissipative particle dynamics method or MARTINI coarse-grained force field (without the more accurate polarizable water model[65]) calculate PMFs that include the exposure of hydrophilic groups/charges to the bilayer core[48–50]. Finally, we again emphasize the importance of free boundary conditions to accommodate the asymmetric insertion of NPs and commensurate curvature generation as discussed at length in the Supplementary Material†. We hope that these methodological considerations prove useful to other researchers interested in modeling NP-bilayer interactions similar to those discussed here.

Our findings indicate that the overall pathway of NP-bilayer fusion involves the approach of a charged, amphiphilic NP to the membrane surface, contact with stochastic lipid tails protrusions or the anchoring of a hydrophobic ligand in the bilayer, then insertion of the NP into the bilayer. In this work we have only considered the insertion of a single NP, effectively neglecting any possible cooperative effects. However, our recent study found that a single embedded NP increases the local likelihood of lipid tail protrusions, indicating that the energy barrier to insertion could be lowered due to cooperative interactions between NPs[34]. Such cooperativity will be a subject of future work. Our past study of insertion of NPs at defect edges also found that charged ligands preferentially distribute with end groups on both sides of the bilayer[15], reflecting the symmetry of the system. At the defect edge there is no barrier to assuming this configuration whereas insertion into the planar bilayers studied here would require charged end groups to translocate through the bilayer to obtain a similar distribution. In future work, we will quantify this barrier for "flipping" charged ligands through the bilayer to achieve a fully membrane-spanning configuration and we postulate that the process may be similar to lipid flip-flop[53]. This work thus yields significant physical insight into this novel protrusion-mediated insertion mechanism and suggests a kinetic pathway for NP-bilayer fusion that may guide the design of novel bio-nano hybrid structures.

Acknowledgments

References

1 A. E. Nel, L. Mädler, D. Velegol, T. Xia, E. M. V. Hoek, P. Somasundaran, F. Klaessig, V. Castranova and M. Thompson, *Nat. Mater.*, 2009, **8**, 543–557.

2 P. Ghosh, G. Han, M. De, C. K. Kim and V. M. Rotello, *Adv. Drug Deliv. Rev.*, 2008, **60**, 1307–1315.

3 D. F. Moyano and V. M. Rotello, *Langmuir*, 2011, **27**, 10376–10385.

4 H.-m. Ding and Y.-q. Ma, *Small*, 2014, DOI: 10.1002/smll.201401943.

5 W. Jiang, B. Y. S. Kim, J. T. Rutka and W. C. W. Chan, *Nat. Nanotechnol.*, 2008, **3**, 145–150.

6 R. Vácha, F. J. Martinez-Veracoechea and D. Frenkel, *Nano Lett.*, 2011, **11**, 5391–5395.

7 J. Lin and A. Alexander-Katz, *ACS Nano*, 2013, **7**, 10799–10808.

8 E. Heikkilä, H. Martinez-Seara, A. A. Gurtovenko, M. Javanainen, H. Häkkinen, I. Vattulainen and J. Akola, *J. Phys. Chem. C*, 2014, **118**, 11131–11141.

9 J. Wong-Ekkabut, S. Baoukina, W. Triampo, I.-M. Tang, D. P. Tieleman and L. Monticelli, *Nat. Nanotechnol.*, 2008, **3**, 363–368.

10 G. von Heijne, *Nat. Rev. Mol. Cell Biol.*, 2006, **7**, 909–918.

11 R. C. Van Lehn, P. U. Atukorale, R. P. Carney, Y.-S. Yang, F. Stellacci, D. J. Irvine and A. Alexander-Katz, *Nano Lett.*, 2013, **13**, 4060–4067.

12 R. P. Carney, Y. Astier, T. M. Carney, K. Voïtchovsky, P. H. Jacob Silva and F. Stellacci, *ACS Nano*, 2013, **7**, 932–942.

13 R. C. Van Lehn and A. Alexander-Katz, *Soft Matter*, 2013, **10**, 648–658.

14 R. C. Van Lehn and A. Alexander-Katz, *J. Phys. Chem. A*, 2014, **118**, 5848–5856.

15 R. C. Van Lehn, M. Ricci, R. P. Carney, K. Voïtchovsky, F. Stellacci and A. Alexander-Katz, *Nat. Commun.*, 2014, **5**, 4482.

16 W. Humphrey, A. Dalke and K. Schulten, *J. Mol. Graphics*, 1996, **14**, 33–38.

17 H. J. Risselada and S. J. Marrink, *Phys. Chem. Chem. Phys.*, 2009, **11**, 2056–2067.

18 L. V. Chernomordik and M. M. Kozlov, *Nat. Struct. Mol. Biol.*, 2008, **15**, 675–683.

19 C. M. Jewell, J.-M. Jung, P. U. Atukorale, R. P. Carney, F. Stellacci and D. J. Irvine, *Angew. Chem. Int. Ed.*, 2011, **50**, 12312–12315.

20 Y.-S. Yang, R. P. Carney, F. Stellacci and D. J. Irvine, *ACS Nano*, 2014, **8**, 8992–9002.

21 O. Lopez-Acevedo, J. Akola, R. L. Whetten, H. Grönbeck and H. Häkkinen, *J. Phys. Chem. C.*, 2009, **113**, 5035–5038.

22 M. Pannuzzo, A. Raudino and R. A. Böckmann, *J. Chem. Phys.*, 2014, **141**, 024901.

23 J. Zimmerberg and M. M. Kozlov, *Nat. Rev. Mol. Cell Biol.*, 2006, **7**, 9–19.

24 D. E. Chandler, J. Gumbart, J. D. Stack, C. Chipot and K. Schulten, *Biophys. J.*, 2009, **97**, 2978–2984.

25 D. E. Chandler, J. Hsin, C. B. Harrison, J. Gumbart and K. Schulten, *Biophys. J.*, 2008, **95**, 2822–2836.

26 A. Arkhipov, Y. Yin and K. Schulten, *Biophys. J.*, 2009, **97**, 2727–2735.

27 A. Arkhipov, Y. Yin and K. Schulten, *Biophys. J.*, 2008, **95**, 2806–2821.

28 H. Yu and K. Schulten, *PLoS Comput Biol*, 2013, **9**, e1002892.

29 K. Yang, B. Yuan and Y.-Q. Ma, *J. Phys. Chem. B*, 2012, **116**, 7196–7202.

30 A. West, K. Ma, J. L. Chung and J. T. Kindt, *J. Phys. Chem. A*, 2013, **117**, 7114–7123.

31 R. C. Van Lehn and A. Alexander-Katz, *J. Phys. Chem. C.*, 2013, **117**, 20104–20115.

32 D. Poger, W. F. van Gunsteren and A. E. Mark, *J. Comput. Chem.*, 2010, **31**, 1117–1125.

33 N. Schmid, A. P. Eichenberger, A. Choutko, S. Riniker, M. Winger, A. E. Mark and W. F. van Gunsteren, *Eur. Biophys. J.*, 2011, **40**, 843–856.

34 R. C. Van Lehn and A. Alexander-Katz, *J. Phys. Chem. B*, 2014, **118**, 12586–12598.

35 D. Poger and A. E. Mark, *J. Chem. Theory Comput.*, 2012, **8**, 4807–4817.

36 B. Hess, *J. Chem. Theory Comput.*, 2008, **4**, 116–122.

37 B. Hess, C. Kutzner, D. van der Spoel and E. Lindahl, *J. Chem. Theory Comput.*, 2008, **4**, 435–447.

38 M. J. Stevens, J. H. Hoh and T. B. Woolf, *Phys. Rev. Lett.*, 2003, **91**, 188102.

39 D. Mirjanian, A. N. Dickey, J. H. Hoh, T. B. Woolf and M. J. Stevens, *J. Phys. Chem. B.*, 2010, **114**, 11061–11068.

40 Y. G. Smirnova, S.-J. Marrink, R. Lipowsky and V. Knecht, *J. Am. Chem. Soc.*, 2010, **132**, 6710–6718.

41 P. M. Kasson, E. Lindahl and V. S. Pande, *PLoS Comput. Biol.*, 2010, **6**, e1000829.

42 C. Chothia, *Nature*, 1974, **248**, 338–339.

43 F. Campelo, H. T. McMahon and M. M. Kozlov, *Biophys. J.*, 2008, **95**, 2325–2339.

44 R. Parthasarathy, C.-h. Yu and J. T. Groves, *Langmuir*, 2006, **22**, 5095–5099.

45 S. Dorairaj and T. W. Allen, *Proc. Natl. Acad. Sci. USA*, 2007, **104**, 4943–4948.

46 R. C. Van Lehn and A. Alexander-Katz, *Soft Matter*, 2011, **7**, 11392.

47 S. Nangia and R. Sureshkumar, *Langmuir*, 2012, **28**, 17666–17671.

48 Y. Li, X. Li, Z. Li and H. Gao, *Nanoscale*, 2012, **4**, 3768–3775.

49 P. Gkeka, L. Sarkisov and P. Angelikopoulos, *J. Phys. Chem. Lett.*, 2013, **4**, 1907–1912.

50 P. Gkeka, P. Angelikopoulos, L. Sarkisov and Z. Cournia, *PLoS Comput Biol*, 2014, **10**, e1003917.

51 S. Kumar, J. M. Rosenberg, D. Bouzida, R. H. Swendsen and P. A. Kollman, *J. Comput. Chem.*, 1992, **13**, 10111021.

52 B. Qiao and M. Olvera de la Cruz, *J. Phys. Chem. Lett.*, 2013, **4**, 3233–3237.

53 N. Sapay, W. F. D. Bennett and D. P. Tieleman, *Soft Matter*, 2009, **5**, 3295–3302.

54 A. Choubey, R. Kalia, N. Malmstadt, A. Nakano and P. Vashishta, *Biophys. J.*, 2013, **104**, 2429–2436.

55 H. Cui, E. Lyman and G. A. Voth, *Biophys. J.*, 2011, **100**, 1271–1279.

56 S. Vanni, L. Vamparys, R. Gautier, G. Drin, C. Etchebest, P. F. J. Fuchs and B. Antonny, *Biophys. J.*, 2013, **104**, 575–584.

57 M. J. Arcario and E. Tajkhorshid, *Biophys. J.*, 2014, **107**, 2059–2069.

58 S. Vanni, H. Hirose, H. Barelli, B. Antonny and R. Gautier, *Nat. Commun.*, 2014, **5**, 4916.

59 L. Vamparys, R. Gautier, S. Vanni, W. F. D. Bennett, D. P. Tieleman, B. Antonny, C. Etchebest and P. J. Fuchs, *Biophys. J.*, 2013, **104**, 585–593.

60 M. Pinot, S. Vanni, S. Pagnotta, S. Lacas-Gervais, L.-A. Payet, T. Ferreira, R. Gautier, B. Goud, B. Antonny and H. Barelli, *Science*, 2014, **345**, 693–697.

61 A. Verma, O. Uzun, Y. Hu, Y. Hu, H.-S. Han, N. Watson, S. Chen, D. J. Irvine and F. Stellacci, *Nat. Mater.*, 2008, **7**, 588–595.

62 H.-Y. Lee, S. H. R. Shin, L. L. Abezgauz, S. A. Lewis, A. M. Chirsan, D. D. Danino and K. J. M. Bishop, *J. Am. Chem. Soc.*, 2013, **135**, 5950–5953.

63 S. Tatur, M. Maccarini, R. Barker, A. Nelson and G. Fragneto, *Langmuir*, 2013, **29**, 6606–6614.

64 G. J. Gordillo, Ž. Krpetić and M. Brust, *ACS Nano*, 2014, **8**, 6074–6080.

65 S. O. Yesylevskyy, L. V. Schfer, D. Sengupta and S. J. Marrink, *PLoS Comput Biol*, 2010, **6**, e1000810.